Nancy McGuire in Noteworthy Chemistry (ACS) Spring 2014

http://www.acs.org/content/acs/en/noteworthy-chemistry/2014-archive/may-26.html#nc1

May 26, 2014

A mixed metal oxide forms a "greener" yellow pigment. Mineral-based pigments are preferable to organic dyes in applications that require long-term stability and heat resistance. Common commercial yellow pigments include $PbCrO_4$, $Pb_2Sb_2O_7$, and CdS, all of which are toxic and face increasing regulatory restrictions.

S. P. Radhika, K. J. Sreeram*, and B. U. Nair at the Council of Scientific and Industrial Research (Chennai, India) prepared an environmentally benign molybdenum-doped gadolinium/cerium oxide yellow pigment. Their procedure consisted of a low-temperature citrate sol–gel process followed by heat treatment (calcination). The resulting pigment particles sizes ranged from nanometers to micrometers (see figure; scale bar is 5 μm).

The authors' process provides good size and shape control for the pigment particles. Introducing Mo^{6+} changes the material from white to dark yellow. The maximum yellow character (less green, more red) was observed at 0.35 mol% molybdenum doping, although the color was yellow at all doping levels between 0.05 and 0.35%. The color did not lighten or darken with doping.

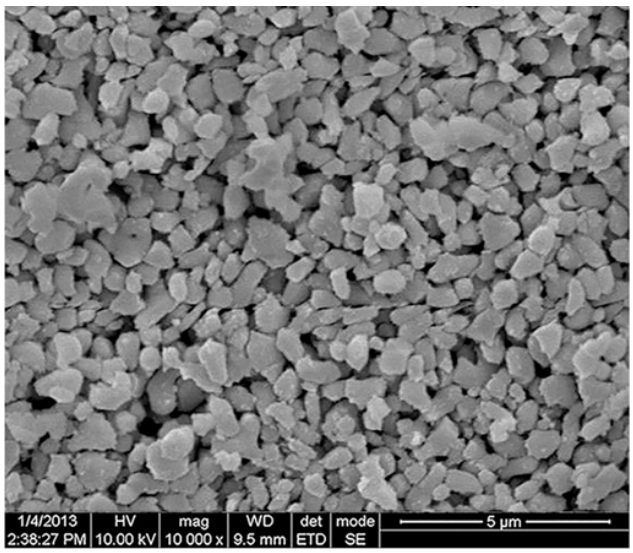

The addition of mineralizers (NaF and $NH_4H_2PO_4$) improved the pigment's ability to cover an underlying color at a lower covering thickness. Mineralizers such as CaF_2, Na_2CO_3, and H_3BO_3 shifted the hue toward orange-yellow.

Near-infrared (NIR) reflectance, an important factor for keeping house and car interiors cool, is ≈70–87% for paints and coatings that contain conventional yellow pigments. The 0.35 mol% Mo-doped pigment showed an NIR reflectance of 91%, possibly because of its particle size and phase structure.

The authors tested the pigment's ability to retain its color when it was dispersed into an alkyd paint medium and when it was incorporated into a poly(methyl methacrylate) solid. The pigment was resistant to acids and alkalis, resisted bleeding into a variety of solvents, and had good light-fastness.

Its stability and the absence of toxic metal ions make the pigment a good candidate for coloring children's toys, home interior finishes, and other applications that involve human contact. (*ACS Sustainable Chem. Eng.* **2014,** *2,* 1251–1256; Nancy McGuire)

http://www.acs.org/content/acs/en/noteworthy-chemistry/2014-archive/may-19.html#nc4

May 19, 2014

Hydrogen bonds affect the growth of reverse micelles around metal ions. Reverse micelles are used for solvent extraction, nanosynthesis, and drug delivery, among other applications. In reverse micelles, a hydrophobic phase surrounds clusters of amphiphilic molecules that encapsulate a hydrophilic phase. Structural studies of metal ions inside reverse micelles have focused on the inner coordination sphere of the metal ions or on the effect of the ions on the nanoscale structure of the micelles, but these two structural scales have not been linked. M. Olvera de la Cruz, R. J. Ellis, and colleagues at Northwestern University (Evanston, IL) and Argonne National Laboratory (IL) used X-ray analysis and molecular dynamics calculations to explain how acidity affects the ways metal atoms connect to the inner surfaces of reverse micelles, and how this affects their size and shape.

The authors examined the interactions that connect "hard" coordinating metal ions to the "soft" cores of reverse micelle aggregates. Their model system consisted of europium nitrate [$Eu(NO_3)_3$] solutions in water or aqueous nitric acid (HNO_3) that are encapsulated in micelles made from *N*,*N*′-dimethyl-*N*,*N*′-dioctylhexylethoxymalonamide and suspended in *n*-heptane.

Increasing the acidity of the system drives hydrogen-bond (H-bond) donor and acceptor molecules (acid and water) into the organic phase, along with increasing concentrations of Eu^{3+}. The Eu^{3+} partitioning ratio was 0.6:1 in the acidic system versus 0.4:1 in the neutral-pH system.

Small-angle X-ray scattering (SAXS) analysis indicates that the micelles have a more elongated shape in the acidic system. There is, however, significant variation in shape: Some clusters are globular and others more rod-shaped. In the neutral system, the micelles tend to be small and spherical.

From the SAXS data, the authors calculated the diameters of the polar reverse micelle cores to be ≈11 and ≈15 Å for the neutral and acidic phases, respectively. This result compares well with diameters of 10.4 and 15.6 Å derived from molecular dynamics calculations.

The figure illustrates typical reverse micelle structures in the neutral system (left) and the acidic system. The large Eu^{3+} ions are shown in pink.

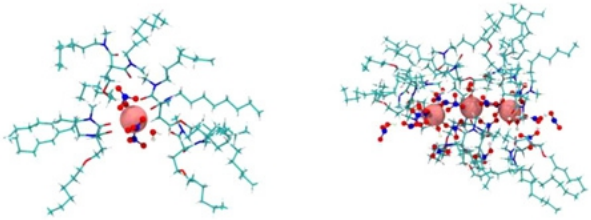

The average number of H-bonds per Eu^{3+} ion is calculated to be 4.17 in the neutral system and 18.4 in the acidic system. In the latter, water and HNO_3 molecules coordinate with the metal ions via H-bonds and dative (coordinate) bonds.

Some of these molecules bond directly with malonamide molecules in the outer sphere. Others form H-bonded chain structures with other water and HNO_3 molecules. These chains form bridges between the Eu^{3+} ions and the malonamide molecules and produce the swollen reverse micelles observed under acidic conditions. (*J. Phys. Chem. Lett.* **2014,** *5,* 1440–1444; Nancy McGuire)

http://www.acs.org/content/acs/en/noteworthy-chemistry/2014-archive/may-12.html#nc6

May 12, 2014

Use supported metal oxide catalysts to synthesize biodiesel. Biodiesel fuel has been around for many years, but the use of strong alkaline reagents to transesterify the plant oil feedstocks hinders its widespread adoption as an automotive fuel source. The best oil feedstocks for use with homogeneous alkaline catalysts contain low levels of free fatty acids. But these oils are also used as food sources; they include soybean, canola, sunflower, rapeseed, and palm oils.

Tree-borne oil seeds, including those from *Jatropha curcas* and *Pongamia pinnata,* are often inedible, even poisonous; but they can be grown on degraded land that is unfit for agricultural production. Oils from these seeds typically contain 5–15% free fatty acids. When the oils are transesterified with homogeneous alkaline catalysts, they tend to form soaps. This complicates the separation and recovery of glycerol from the resulting biodiesel fuel.

S. Mahajani and co-workers at the Indian Institute of Technology Bombay (Mumbai) developed a method that uses supported metal oxide catalysts for making biodiesel from jatropha oil. Their evaluation of ZnO and PbO catalysts on zeolite substrates showed that both catalysts have reasonably good activity and can be reused under the reaction conditions. Excess methanol was added to the reaction mixture to accelerate the reaction and increase the conversion of oil to biodiesel.

The authors used ZSM-5 zeolite, β-zeolite, α-alumina, or γ-alumina as the catalyst supports. Because of the high Si/Al ratios (low acidities), these supports showed no catalytic activity on their own. The zeolites minimized metal-ion leaching during the reaction, an important environmental consideration. Alumina did not bind the metal oxides as strongly as the zeolites, and it released more metal ions during the reaction.

The PbO/zeolite catalyst performed especially well for oils with <1 wt% free fatty acids. For PbO/ZSM-5, triglyceride conversion was almost 100% after 30 min. The ZnO/zeolite catalyst was better for feedstocks that contained >10 wt% free fatty acids; it also worked well with oleic acid.

The fatty acid methyl ester yields with ZnO/zeolite and PbO/zeolite were ≈94% and >90%, respectively. The reactions were run at 200 °C, an oil/MeOH mol ratio of 1:30, 1 h reaction time, and a catalyst loading of 1.0 wt% (ZnO) or 0.5 wt% (PbO). (*Energy Fuels* **2014,** *28,* 2743–2753; Nancy McGuire)

http://www.acs.org/content/acs/en/noteworthy-chemistry/2014-archive/may-5.html#nc2

May 5, 2014

What do sugarcane juice and azo dyes have in common? Photocatalysts are useful for degrading organic pollutants, but preparing nanoparticles of these materials typically involves energy- and capital-intensive methods that use harsh or toxic chemical reagents. These factors counterbalance the sustainability of the photocatalysts. A greener synthesis method would avoid the use of solvents and stoichiometric reagents, limit waste production, and use available, renewable resources.

A. A. Kulkarni and B. M. Bhanage* at the Institute of Chemical Technology (Mumbai, India) developed a method that uses sugarcane juice to produce AgCl nanoparticles with doped silver on their surfaces (Ag@AgCl). They used these particles to promote the visible-light photocatalytic degradation of two azo dyes, methyl orange and methylene blue, in aqueous solution. The catalyst can be reused as many as four times without significant loss of catalytic activity.

The authors call sugarcane juice "a bag full of reducing agents (glucose), well-known capping agents (organic acids), and halide ion sources (chloride ion) that can be utilized for preparation of nanomaterials". They dissolved $AgNO_3$ in sugarcane juice and heated the mixture at 80 °C for 20 min to produce Ag@AgCl particles with an average size of 37 nm. They determined that the sugarcane juice plays a key role in producing well-dispersed, uniform particles and reducing the AgCl to form elemental silver on the particle surfaces. This silver activates the catalyst by absorbing visible light and transferring electrons to the AgCl conduction band.

The authors added 100 mg of the nanoparticles to 25 mL of dye solution and allowed the mixture to stand in the dark for 1 h. They observed an adsorption−desorption equilibrium of the dye on the catalyst surface. They then irradiated the mixture with UV-free visible light from a quartz halogen lamp.

The catalyst was removed via centrifugation, and the degree of dye degradation was measured with UV−vis spectroscopy. Methyl orange is completely degraded after 21 min; 50 min is required for methylene blue. (*ACS Sustainable Chem. Eng.* **2014,** *2,* 1007–1013; Nancy McGuire)

http://www.acs.org/content/acs/en/noteworthy-chemistry/2014-archive/april-28.html#nc3

April 28, 2014

Gelation is a promising method for removing mercury. The stimulus-responsive behavior of molecular gels makes them promising candidates for environmental remediation operations. Gel-based materials respond to metal ions, reductants, oxidants, and enzymes, but predicting which molecules will form gels is a challenge.

K. K. Carter, H. B. Rycenga, and A. J. McNeil* at the University of Michigan (Ann Arbor) examined a series of mercury-containing compounds to elucidate the relationship between their chemical structures and their ability to form gels. They found a complex relationship between the chemical structures and properties of these compounds, but they established that gel formation can remove >98% of Hg^{2+} from contaminated water.

Under the assumption that the 1-D interactions drive the growth of gel fibers, the authors used the Cambridge Structural Database to identify molecules that exhibit 1-D intermolecular interactions in the solid state, specifically Hg–arene interactions. They found a promising candidate in compound **1** and tested three derivatives of this compound (**2**, **3**, and **4** in the figure) for their ability to form gels in mixtures of water and organic solvents.

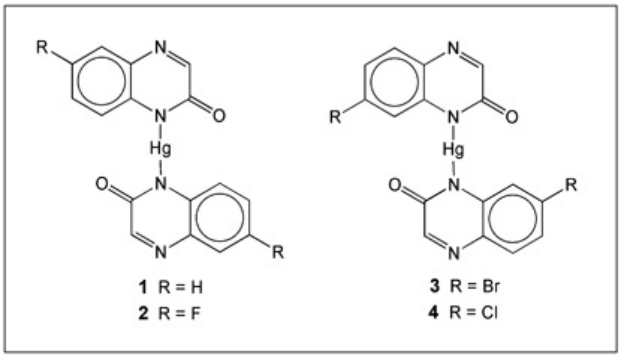

The usefulness of **1** is limited because high concentrations of the gelator and an organic cosolvent are required. In addition, the gel dissolves rapidly in the presence of chloride ion. One of its derivatives (**3**) removes >99% of the Hg^{2+} from water at lower concentrations, and it is insensitive to Cl^{-}.

Gel formation appears to be more sensitive to the position and identity of the substituents than to the quinoxalinone framework. The authors examined the solubility properties of their nine compounds in MeOH and EtOH at various temperatures. They found that all the compounds undergo a solid–solid transformation in MeOH, and some do the same in EtOH. The variety of polymorphs observed and the lack of a solvent that works for all the compounds complicated comparisons among structurally similar gelators and nongelators.

The authors added $Hg(OAc)_2$ to bottled water, tap water, and water from the Huron River. They mixed the mercury-contaminated water with MeOH solutions that contained quinoxalinone compounds and observed instantaneous gel formation. All of the gelators removed >98% of the Hg^{2+} from the water. Gel formation is selective for Hg^{2+} in the presence other metal ions. Gels do not form in water to which no $Hg(OAc)_2$ is added. (*Langmuir* **2014,** *30,* 3522–3527; Nancy McGuire)

http://www.acs.org/content/acs/en/noteworthy-chemistry/2014-archive/april-21.html#nc7

April 21, 2014

Mine residues are oxygen carriers for biomass fuel processing. Biomass fuels are often pretreated by using a mild form of pyrolysis to release water and volatiles in a process called torrefaction. The result is a dry, energy-dense product that is not subject to rotting. Integrated torrefaction uses the volatiles released from the biomass itself as the fuel source, but these volatiles must be processed first to prevent combustion and uneven heating.

A. Sarvaramini and F. Larachi* at Laval University (Quebec City) report a method for processing gas emitted during torrefaction that uses magnesium iron silicate residues from a nickel mining operation. The mineral residue provides an abundant, inexpensive source of solid oxygen carriers (iron oxides) for chemical looping combustion (CLC). The magnesium forms carbonates that act as a carbon sink.

The authors found that almost all of the carbon released during CLC is converted to CO_2. A subsequent carbonation reaction captures as much as 20% of this CO_2. The figure shows a schematic drawing of the combined procedures.

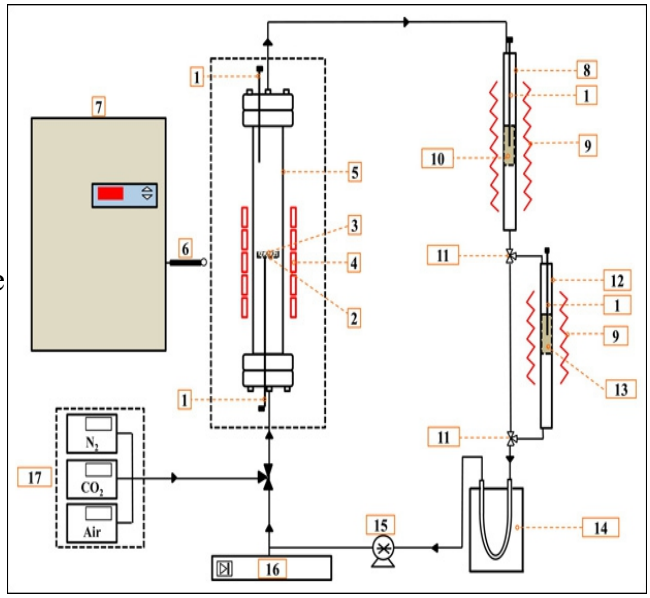

Birch wood chips are torrefied under an oxygen-free nitrogen atmosphere. The released volatiles flow into a CLC reactor vessel that contains mine residue particles—17.3 wt% Fe, 13.8 wt% Mg, and 16.5 wt% Si—in the 100−250 μm size range. Before use, the residue was air-calcined to increase the extra-framework oxidized iron content. This reactor burns the volatiles in the flue gas to produce CO_2 and water. The authors reused the residue particles for as many as five consecutive oxidation−reduction cycles without a significant loss of activity.

The effluent from the CLC passes into a third vessel that contains magnesium-rich material leached from spent calcined mineral residues. This material has ≈50% of its pore volume filled with water, into which the CO_2 from the flue gas dissolves. The solution reacts with the magnesium to form solid carbonates. The gas that leaves this reactor passes through a cold trap to collect water and condensable volatiles, and the remaining CO_2, CO, hydrogen, and methane are recirculated to the torrefaction vessel to serve as fuel for the pyrolysis process.

The authors note that other mine residues they tested produced more carbonates, probably because they had a higher content of free magnesium oxides. The reaction rate increases with temperature, but increasing the temperature to >50 ºC causes the water to evaporate, which impedes the carbonation reaction. (*Energy Fuels* **2014,** *28,* 1983–1991; Nancy McGuire)

http://www.acs.org/content/acs/en/noteworthy-chemistry/2014-archive/april-7.html#nc5

April 7, 2014

Suspend free-standing 2-D iron sheets in graphene pores. Theoretical studies predict that the magnetic moment of a free-standing iron monolayer is 3.1 μB, as compared with 2.2 μB measured for bulk iron. This value is important in several applications, including magnetic recording media. Materials such as graphite, BN, and MoS_2 have strongly directional bonding and readily form free-standing sheet structures. Metals, however, form chemical bonds in all directions. Until now, the only examples of atomically thin metal sheets were heteroepitaxial layers attached to a substrate.

M. H. Rümmel and co-workers at the Institutes of Complex Materials, Solid State Research, and Materials Science (Dresden, Germany), the Institute for Basic Science (Daejon, Korea), the Polish Academy of Sciences (Zabrze), and Sungkyunkwan University (Suwon, Korea) formed free-standing, one-atom-thick iron sheets in the pores of graphene sheets. They used chemical vapor deposition to grow graphene on Ni–Mo substrates then detached the graphene layers by using an $FeCl_3$ etching solution, which introduced several forms of iron.

Transmission electron microscopy (TEM) showed pure iron crystalline layers, one atom thick, suspended across perforations in the graphene sheets. Other species include body-centered cubic and hexagonal close-packed iron nanocrystals, several-atom clusters, and individual iron atoms attached to the graphene edges.

All of the monoatomic iron layers that the authors examined showed a preferential alignment of the iron (110) plane with the graphene (1–100) plane. The observed lattice constant is 2.65 Å, whereas the most stable lattice constant calculated from using density functional theory is 2.35 Å. The calculated energy difference between the two values, however, is only 0.2 eV/atom. Several factors, including spin–orbit coupling, perpendicular magnetic anisotropy, and strain produced by lattice alignment and mismatch between iron and graphene, are likely to affect the lattice constant value.

The researchers studied the modes of attachment between the iron and graphene and examined the local strain effects. They observed that iron almost always binds to open graphene edges. One iron atom generally substitutes for one carbon atom in a benzene ring, although other configurations occur as well. The researchers calculated that the largest stable crystalline monolayer is ≈12 atoms across, or 3 nm on a side. The largest crystalline monolayers that they observed were ≈10 atoms across.

When irradiated by the TEM beam, iron atoms on the graphene surface move around and collect in small holes, where they form crystalline monolayers within a few seconds. These monolayers are stable for several minutes under electron radiation; they then begin to collapse to form amorphous particles. (*Science* **2014,** *343,* 1228–1232; Nancy McGuire)

http://www.acs.org/content/acs/en/noteworthy-chemistry/2014-archive/march-31.html#nc1

March 31, 2014

UN assesses the effects of the Fukushima nuclear accident on wildlife. On March 11, 2011, an earthquake-generated tsunami struck the Fukushima-Daiichi Nuclear Power Station in Japan. The tsunami caused a catastrophic failure and a release of radioactive material that has been rated second in magnitude only to the Chernobyl disaster. The extent of the radiological impact of this event on surrounding wildlife has been a contentious topic.

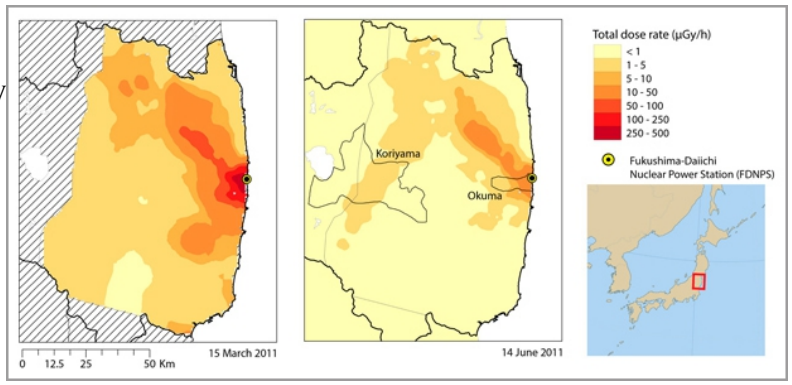

P. Strand, T. Aono, and coauthors at the Norwegian Radiation Protection Authority (Østerås, Norway), the Norwegian University of Life Sciences (Ås), the National Institute of Radiological Sciences (Chiba, Japan), the Institute for Radioprotection and Nuclear Safety (Saint Paul lez Durance, France), the State Institution Research and Production Association Typhoon (Obninsk, Russian Federation), the University of Groningen (The Netherlands), and Biosphere Impact Studies (Mol, Belgium) evaluated an assessment, overseen by the UN Scientific Committee on the Effects of Atomic Radiation, in which a suite of recently developed techniques was applied to calculate the radiation exposure of regional wildlife. The UN committee compiled monitoring data for the year following the accident; relevant reports and scientific papers provided additional data. Radiation effects were inferred by comparing compiled dose−response relationships.

Radiation exposures were evaluated for the first 3 months after the accident, during which short-lived isotopes played a significant role, and for a later phase (3–12 months), in which exposure was dominated by longer-lived isotopes. Radionuclide concentrations were measured over time and geographic area. Kinetic models were used to calculate time-dependent concentrations in biota. Cumulative doses were determined from dose calculations.

Adult butterflies collected in September 2011 showed more severe abnormalities than those collected in May 2011, indicating deterioration in the population caused by cumulative exposure effects; but dosimetry uncertainties and other confounding factors complicate the interpretation of these observations. The main body of scientific data does not support the appearance of these effects at the dose rates recorded. Reproducing these effects under laboratory conditions required radiation exposures orders of magnitude greater than those observed in the field. Declines in some bird populations and exposures of macroalgae that exceeded corresponding benchmarks also point to possible localized effects.

The team concludes that, because of the short duration of the highest exposure levels, there was likely no damage to the population integrity of plant and animal species. Individual organisms in relatively contaminated areas might have been damaged during the weeks immediately after the accident, especially individuals of radiosensitive and sedentary species living in high-deposition areas.

The figure shows an interpolated map of total weighted absorbed dose rates for a large mammal on March 15 and June 15, 2011. The calculations were based on empirical ^{131}I, ^{134}Cs, and ^{137}Cs soil-deposition data measured in June and July 2011 that were converted to soil concentrations and corrected for radioactive decay to mid-March 2011. During the late phase, individuals of some species, especially mammals, faced potential risks in limited areas. Entire populations are unlikely to suffer significant exposure effects. (*Environ. Sci. Technol. Lett.,* **2014,** *1,* 198–203; Nancy McGuire)

http://www.acs.org/content/acs/en/noteworthy-chemistry/2014-archive/march-24.html#nc3

March 24, 2014

Silica and germania bond angles have diverse energy minima. Zeolite researchers often search databases of hypothetical structures for potentially useful configurations to synthesize. Energy optimization calculations help them select hypothetical structures that are most likely to be stable and practical to make. Zeolite models that use rigid TO_4 tetrahedra (in which T is a generic tetrahedrally coordinated atom) connected at the oxygen vertices by force-free spherical joints are consistent with experimental data.

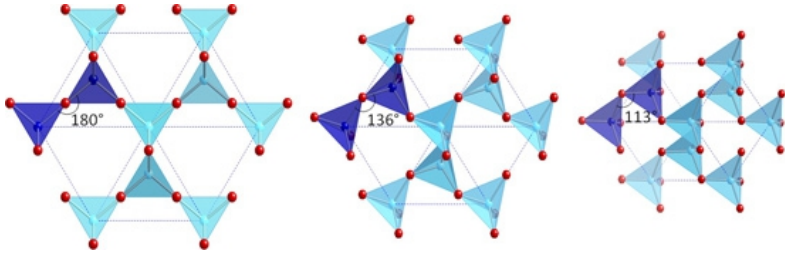

Ab initio calculations that compare the energy dependence of Si−O−Si and Ge−O−Ge bond angles suggest that the most stable structures for silicas are not necessarily the same as those for germanias. Several cluster models for germania structures have been studied, but M. M. J. Treacy and coauthors at Arizona State University (Tempe) and KAIST (Daejeon, Korea) believe that their study is the first to use a crystalline lattice model for the energy dependence of Ge−O−Ge angles. They calculated the energy dependence for the quartz and cristobalite structures and then extended their model to several known zeolite structures. The figure shows the transformation of the T−O−T angles in a calculated cristobalite structure from 180º to 113º.

Silica and germania exhibit markedly different results for calculated energies over the range of T−O−T angles studied (120º–180º), but all of the energy curves for silica structures were similar, as were the curves for germania structures. The energy for silica structures decreases sharply as the T−O−T angle increases from 120º to 140º and then remains relatively constant up to 180º.

Germania structures exhibit an energy minimum at ≈128º−130º, and the energy rises steadily as the T−O−T angle increases to 180º. The energy penalty calculated when the full lattice model is used is even greater than that reported in previous cluster-model studies. For the economically important zeolite faujasite framework, the minimum range of T−O−T angles (141º−144º) is well within the stable range for silica, but probably prohibitive for germania.

The authors note that, of the 5824 low-energy frameworks described in the Atlas of Prospective Zeolite Structures, 48 have all of their T−O−T angles in the most favorable range for germania (117º−145º), but 994 lie in the optimal range for silica (135º−180º). Mixing germanium and silicon in the framework could extend the range of stable bond angles and increase the number of stable structures available for synthesis. (*Chem. Mater.* **2014,** *26,* 1523–1527; Nancy McGuire)

http://www.acs.org/content/acs/en/noteworthy-chemistry/2014-archive/march-17.html#nc6

March 17, 2014

These optical waveguides can bend and stretch. Flexible, stretchable electronic materials have led to applications such as sensitive robotic skin, wearable sensing devices, and monitoring systems for moving machine parts. Similar flexible optical devices, however, are at a much earlier stage of development. Preparing stretchable optical interconnects is problematic because most conventional optical waveguide materials have limited or no flexibility.

J. Missinne and co-workers at the Center for Microsystems Technology (Ghent, Belgium) and Ghent University used commercially available polydimethylsiloxane (PDMS) materials to produce optical waveguides that bend and stretch. PDMS with a refractive index of 1.57 is introduced via capillary filling into channels in a cladding material that was made from another PDMS polymer with a 1.41 refractive index. As the refractive index difference between core and cladding increases, the achievable bending radius of the resulting waveguide decreases.

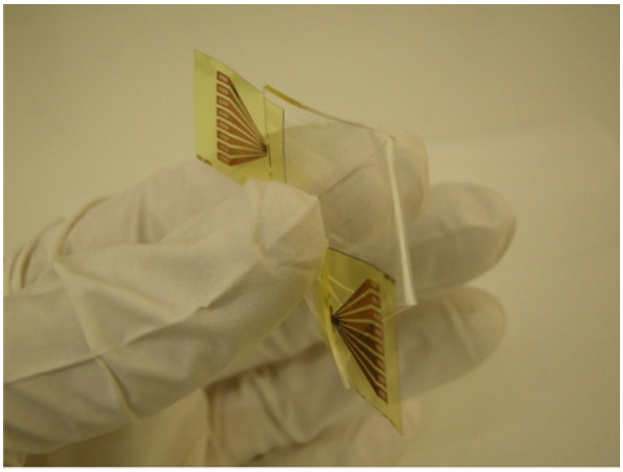

Courtesy of the Optical Society.

Because actively aligning light sources and detectors at the input and output ends of a bending optical fiber is difficult, the authors devised a process for producing waveguides with integrated optoelectronic components. They embedded thinned, bare-die vertical-cavity surface-emitting lasers (VCSELs, $\lambda = 850$ nm) and photodiodes in flexible polyimide foils and coupled the foils to 50 μm x 50 μm x 6 cm waveguide arrays. The figure shows the bending of the complete assembly.

The authors characterized the waveguide assemblies by measuring propagation, stretching, and bending losses and reliability. The total link loss, including coupling loss, is 2–4.5 dB. Waveguide losses are negligible (≤0.1 dB) for bending radii as small as 7 mm. Stretching the waveguide regions by as much as 30% and subsequently releasing them contributes <0.7 dB to the total optical link loss.

Stretching the waveguides by >30% causes stability problems in the coupling region, but the waveguide substrate can be stretched as much as 140% before the PDMS material breaks. After 80,000 stretching cycles at 10% elongation, the small long-term average insertion loss indicates that stretching does not introduce noticeable degradation. (*Opt. Express* **2014,** *22*, 4168–4179; Nancy McGuire)

http://www.acs.org/content/acs/en/noteworthy-chemistry/2014-archive/march-10.html#nc1

March 10, 2014

Lycopene effectiveness gets a boost. Lycopene, a carotenoid found in tomatoes, is associated with a decreased risk of cardiovascular disease and certain cancers, and it has been shown to exhibit antioxidant properties. Dried tomato peel and tomato powder can be added as a nutritional supplement to ready-to-eat meat products without the need for chemical extraction of the lycopene component.

All-(*E*)-Lycopene accounts for 80–97% of the lycopene isomers in tomatoes and related products, but various *Z*-forms account for 25–70% of the lycopene in human tissues and body fluids. Some *Z*-isomers show stronger antioxidant activity in vitro than the all-*E* form.

M. M. Calvo, and coauthors at Complutense University and the Institute of Food Science Technology and Nutrition (both in Madrid) and Friedrich Schiller University Jena (Germany), and Catholic University School of Medicine (Rome) studied the effects of electron-beam (e-beam) irradiation, a common meat sterilization method, on the isomerization and degradation of lycopene additives from dried tomato products. They centrifuged and dried ground fresh tomatoes to obtain the powder, and they freeze-dried the peels. Both products were sealed in low-permeability packaging and irradiated at 10 MeV and 4 kGy at an electron accelerator facility. Temperatures were held to <18 °C, and the samples were protected from light.

The results showed that dried tomato peel has almost twice the lycopene content (0.2 ± 0.02 mM) of the powder (0.1 ± 0.01 mM). Irradiation exposure reduced the lycopene content by ≈50% for both products. HPCL analysis of the peel and powder showed a reduction of all-(*E*)-lycopene and an increase in (*Z*)-lycopene isomers during irradiation. This effect was significantly stronger in the peel samples than in the powders.

The authors used RAT-1 fibroblasts to check for antioxidant activity, which they measured as the lycopene's ability to inhibit intracellular reactive oxygen species (ROS), with and without the prooxidant agent H_2O_2. A weak, but significant, inhibition of ROS production was observed when the fibroblasts were treated with the tomato products in the absence of H_2O_2. The inhibition effect was stronger for cells incubated with H_2O_2.

The tomato extracts also inhibited the phosphorylation of mitogen-activated protein kinases, which are associated with stress stimuli, including ROS production. Adding tomato extracts inhibited the expression of the oxidative stress-sensitive transcription factor NF-κB and the oxidative stress–signaling proteins cyclooxygenase-2 and nicotinamide adenine dinucleotide phosphate oxidase.

In all cases, the effect was stronger for peels than for powder extracts and more evident for irradiated samples than for nonirradiated ones. The effects were more pronounced for larger doses of the tomato extracts. All of the effects were observed for a range of carotenoid concentrations that can be reached in vivo after lycopene or tomato supplementation. (*J. Agric. Food Chem.* **2014,** *62,* 1557–1563; Nancy McGuire)